Systems/Circuits

Spontaneous Spiking Is Governed by Broadband Fluctuations

Zachary W. Davis,[1] Lyle Muller,[2,3] and John H. Reynolds[1]

[1]Salk Institute for Biological Studies, La Jolla, California 92037, [2]Department of Applied Mathematics, Western University, London, Ontario N6A 3K7, Canada, and [3]Brain and Mind Institute, Western University, London, Ontario N6A 3K7, Canada

Populations of cortical neurons generate rhythmic fluctuations in their ongoing spontaneous activity. These fluctuations can be seen in the local field potential (LFP), which reflects summed return currents from synaptic activity in the local population near a recording electrode. The LFP is spectrally broad, and many researchers view this breadth as containing many narrowband oscillatory components that may have distinct functional roles. This view is supported by the observation that the phase of narrowband oscillations is often correlated with cortical excitability and can relate to the timing of spiking activity and the fidelity of sensory evoked responses. Accordingly, researchers commonly tune in to these channels by narrowband filtering the LFP. Alternatively, neural activity may be fundamentally broadband and composed of transient, nonstationary rhythms that are difficult to approximate as oscillations. In this view, the instantaneous state of the broad ensemble relates directly to the excitability of the local population with no particular allegiance to any frequency band. To test between these alternatives, we asked whether the spiking activity of neocortical neurons in marmoset of either sex is better aligned with the phase of the LFP within narrow frequency bands or with a broadband measure. We find that the phase of broadband LFP fluctuations provides a better predictor of spike timing than the phase after filtering in narrow bands. These results challenge the view of the neocortex as a system composed of narrowband oscillators and supports a view in which neural activity fluctuations are intrinsically broadband.

Key words: **brain rhythms; broadband; cortical dynamics; marmoset; oscillations; spontaneous activity**

Significance Statement

Research into the dynamical state of neural populations often attributes unique significance to the state of narrowband oscillatory components. However, rhythmic fluctuations in cortical activity are nonstationary and broad spectrum. We find that the timing of spontaneous spiking activity is better captured by the state of broadband fluctuations over any latent oscillatory component. These results suggest narrowband interpretations of rhythmic population activity may be limited, and broader representations may provide higher fidelity in describing moment-to-moment fluctuations in cortical activity.

Introduction

Since the first human electroencephalogram (EEG) recordings by Hans Berger (Berger, 1929), neuroscientists have inferred cortical function from the state of rhythmic fluctuations in neural population activity (Buzsáki and Draguhn, 2004; Wang, 2010). These brain rhythms are believed to arise from return currents generated by large-scale spiking activity in cortical neural populations (Logothetis, 2003; Katzner et al., 2009; Buzsáki et al., 2012). When recorded intracranially with penetrating electrodes, rhythmic activity can be measured in the local field potential (LFP), which typically reflects neural signals arising within ~250 μM of the electrode tip (Katzner et al., 2009; Lindén et al., 2011). LFP fluctuations are spectrally broad but are often thought to be composed of activity in narrow frequency bands correlated with distinct neural functions (Canolty et al., 2010; Einevoll et al., 2013; Friston et al., 2015). For example, in the visual cortex, alpha band rhythms (8–15 Hz) are thought to reflect feedback processes of suppression (Jensen and Mazaheri, 2010; van Kerkoerle et al., 2014) and have been shown to be attenuated with or modulated by attention (Worden et al., 2000; Busch and VanRullen, 2010). Beta band rhythms (15–30 Hz) have been linked to motor planning (Sanes and Donoghue, 1993; Rubino et al., 2006) and feedback regulation of excitability (Bastos et al., 2015; Friston et al., 2015). Theta band (4–8 Hz) activity has been related to attention (Fiebelkorn and Kastner, 2019), working memory load (Jensen and Tesche, 2002), and hippocampal function (Buzsáki, 2002). Delta band (<4 Hz) activity has been related to sleep and states of arousal (Sanes and Donoghue, 1993; Steriade et al., 2001;

Received Sep. 19, 2021; revised Apr. 26, 2022; accepted Apr. 28, 2022.

Author contributions: Z.W.D., L.M., and J.H.R. designed research; Z.W.D. performed research; L.M. contributed unpublished reagents/analytic tools; Z.W.D. analyzed data; Z.W.D. and J.H.R. wrote the paper.

This work was supported by the Gatsby Charitable Foundation; the Fiona and Sanjay Jha Chair in Neuroscience; the Canadian Institute for Health Research; the Swartz Foundation; National Institutes of Health Grants R01-EY028723, T32 EY020503-06, T32 MH020002-16A, and P30 EY019005; NSF (NeuroNex Grant No. 2015276); and BrainsCAN at Western University through the Canada First Research Excellence Fund. We thank Katie Williams, Sean Adams, Mat LeBlanc, and Tom Franken for contributions to this project.

The authors declare no competing financial interests.

Correspondence should be addressed to John H. Reynolds at reynolds@salk.edu or Zachary W. Davis at zdavis@salk.edu.

https://doi.org/10.1523/JNEUROSCI.1899-21.2022

McGinley et al., 2015). Higher frequency gamma activity (30–90 Hz) has been linked to local coordination in excitation and inhibition (Brunel and Wang, 2003; Bartos et al., 2007; Buzsáki and Wang, 2012), attention (Fries et al., 2001, 2008; Gregoriou et al., 2009), memory (Pesaran et al., 2002; Colgin et al., 2009; van Vugt et al., 2010; Lundqvist et al., 2018), and perception (Singer and Gray, 1995; Panagiotaropoulos et al., 2012; Misselhorn et al., 2019), and has been used as a surrogate for measuring cortical activation (Crone et al., 2006; Ray et al., 2008a; Merker, 2013). Oscillatory activity can be induced under certain conditions, such as the increased low-frequency power that is observed in the EEG when eyes are closed (Berger, 1929; Geller et al., 2014), optogenetically (Lu et al., 2015; Bitzenhofer et al., 2017; Zutshi et al., 2018), electrically (Contreras et al., 1997; Kirov et al., 2009; Escobar Sanabria et al., 2020), or pharmacologically as in the alpha oscillations that occur in medial prefrontal cortex under propofol-induced anesthesia (Purdon et al., 2013; Flores et al., 2017; Bastos et al., 2021).

It has been proposed that certain frequency bands play a privileged role in routing information among brain areas (Akam and Kullmann, 2010; Bonnefond et al., 2017; Khamechian et al., 2019). The idea that communication between brain areas occurs through oscillatory processes within narrow frequency bands bears similarity to a radio, where signals are broadcast within different frequency bands and a receiver can be tuned to receive them (Hoppensteadt and Izhikevich, 1998). For example, the idea of cross-cortical communication through coherence views synchrony in gamma oscillations as periods of coordination between presynaptic and postsynaptic groups to transmit signals about, for example, an attended stimulus while blocking competing inputs (Fries, 2015). These patterns of gamma-band synchronization are proposed to be regulated across cortical areas by top-down signals within a slower (8–20 Hz) frequency band (Bastos et al., 2015). Other theories suggest that the LFP is composed of multiplexed oscillatory neural signals that are separate streams of information processing (Lisman and Idiart, 1995; Panzeri et al., 2010; Akam and Kullmann, 2014; Tingley et al., 2018). If oscillatory activity in separate frequencies encodes distinct information channels, and the spiking activity of neurons are the fundamental units of information transmission in the nervous system, then the spiking activity of individual neurons should show preferential alignment of their spiking activity to oscillatory rhythms to tune in to a channel of information (Canolty et al., 2010; Belluscio et al., 2012). There is evidence to suggest this can occur, as spikes have been found to preferentially align with the phase of theta (Takahashi et al., 2014; Souza and Tort, 2017; Strüber et al., 2022), alpha (Haegens et al., 2011), gamma (Fries et al., 2001; Womelsdorf et al., 2007; Ray et al., 2008b), and beta (Donoghue et al., 1998; Canolty et al., 2010) frequencies.

An alternative view is that neurons spike with no preference for any particular narrowband frequency. Rather, spiking is modulated by the instantaneous state of fluctuations in the local population, which varies from moment to moment across a broad range of frequencies. Supporting this view is the observation that balanced excitation and inhibition creates fluctuating neural activity patterns in the awake state, which often exhibit $1/f^{\alpha}$ power spectra across a broad range of frequencies (Destexhe et al., 2001; Gao et al., 2017). Studies in humans have found that changes in cognitive state are associated with broad spectral changes in the EEG (Voytek et al., 2015). The membrane potential of individual neurons is correlated with the population fluctuations measured in the instantaneous LFP (Haider et al., 2016), as opposed to any narrowband component, which suggests the broadband LFP is therefore informative about the instantaneous excitability of neurons in the population (Davis et al., 2020). Accordingly, previous work has found that spikes are weakly coupled to all frequencies of the broadband LFP (Martin and Schröder, 2016), and specific interactions in narrowband frequencies may at times be because of spurious artifacts from narrowband filtering (Scheffer-Teixeira and Tort, 2016).

Even when approximately oscillatory activity may be transiently apparent in LFP recordings, it is difficult to describe the phase of neural fluctuations within a narrow range of frequencies because of their nonstationarity (Pesaran et al., 2018). LFP phase is a useful measure for tracking the state of neural fluctuations because it is indicative of the relative transition in the balance of excitation and inhibition with, for example, the falling phase reflecting a transition from inhibition to excitation, and the rising phase transitioning from excitation to inhibition (Atallah and Scanziani, 2009; Poo and Isaacson, 2009; Isaacson and Scanziani, 2011; Teleńczuk et al., 2017). This is in contrast to amplitude measures, which can be ambiguous as the same negative voltage value could reflect neurons becoming more depolarized or more hyperpolarized depending on the signal history. Under this view, one can better characterize the state of neural populations from the phase of broadband fluctuations in LFP activity, and neurons will show preferential alignment of their spiking activity to the broadband signal phase, not to any narrowband oscillatory phase.

To ask whether neuronal spiking is better coupled to narrowband oscillations or broadband fluctuations during waking visual function, we compared spike-phase coupling after filtering the LFP in various filter bands. If the spiking probability of a neuron is phase locked with the LFP within some frequency band, this is evidence that the neuron in question participates, to some degree, in oscillatory activity of the larger ensemble of neurons whose transmembrane currents give rise to that rhythm. If narrowband rhythms do reflect distinct information channels, then the phase of these oscillations should be particularly informative about the excitability of neurons participating in that oscillatory rhythm and therefore the timing of their spontaneous spiking activity. Alternatively, if the excitability of the population is reflected in the phase of the broad spectrum fluctuations, then the spiking activity of neurons should be more poorly predicted by any individual oscillatory component and better predicted by the phase of the broadband LFP. Therefore, in this work we take the magnitude of spike-phase coupling as a direct measure of the degree to which oscillatory activity reflects a discrete information channel.

The ability to test between these alternatives has been limited, however, because the calculation of phase using the Hilbert transform breaks down when the frequency content of a signal is too broad (Le Van Quyen et al., 2001). It had been infeasible to directly compare the relative phase coupling of spiking activity to narrowband or broadband LFP signals without consideration of this potential confound. To overcome this technical limitation, we have developed a measure of phase [generalized phase (GP); Davis et al., 2020], a generalization of the Hilbert transform that can be applied to spectrally broad signals, allowing us to directly compare narrowband and broadband phase estimates of cortical excitability. This enabled us to test whether the timing of spontaneous spiking activity in cortical populations is better aligned with the phase of classically defined narrowband oscillations, similar to channels on a radio, or is more tightly coupled to the phase of the broad ensemble of nonstationary components. In recordings made from the marmoset middle temporal (MT)

extrastriate visual cortex, we find that spontaneous spiking is more strongly phase coupled to the broadband LFP than to any individual narrow band. Thus, fluctuations in spontaneous neuronal spiking are not coupled preferentially to individual narrowband oscillations but rather track with the instantaneous fluctuations of neural activity as they change from moment to moment.

Materials and Methods

Electrophysiology recordings. One male (monkey W) and one female (monkey T) marmoset monkey (*Callithrix jacchus*) were surgically implanted with a headpost for head stabilization and eye tracking. The headpost contained a hollow chamber housing an Omnetics connector for a Utah array (Blackrock Microsystems), which was implanted in a 7 × 10 mm craniotomy over area MT (stereotaxic coordinates, 2 mm anterior, 12 mm dorsal). An 8 × 8 (64 channel, monkey W) and 9 × 9 with alternating channels removed (40 channel, monkey T) Utah array was chronically implanted over area MT using a pneumatic inserter wand. The electrode spacing was 400 μM with a pitch depth of 1.5 mm. The craniotomy was closed with DuraSeal (Integra Life Sciences, monkey W) or DuraGen (Integra Life Sciences, monkey T), and covered with a titanium mesh embedded in dental acrylic. All surgical procedures were performed with the monkeys under general anesthesia in an aseptic environment in compliance with National Institutes of Health guidelines. All experimental methods were approved by the Institutional Animal Care and Use Committee of the Salk Institute for Biological Studies and conformed with National Institutes of Health guidelines. Data used in this study were previously used in Davis et al. (2020).

Marmosets were trained to enter a custom-built marmoset chair that was placed inside a Faraday box with an LCD monitor (ASUS VG248QE) at a distance of 40 cm. The monitor was set to a refresh rate of 100 Hz and gamma corrected with a mean gray luminance of 75 candelas/m^2. Electrode voltages were recorded from the Utah arrays using two Intan Technologies RHD2132 amplifiers connected to an Intan Technologies RHD2000 USB interface board. Data were sampled at 30 kHz from all channels. The marmosets were head fixed by a headpost for all recordings. Eye position was measured with an ISCAN CCD infrared camera sampling eye position at 500 Hz. Stimulus presentation and behavioral control was managed through MonkeyLogic (Asaad et al., 2013) in MATLAB. Digital and analog signals were coordinated through National Instruments DAQ cards (catalog #PCI6621) and BNC breakout boxes (catalog #BNC2090A, National Instruments). Neural data were broken into two streams for offline processing of spikes (single-unit and multiunit activity) and LFPs. Spike data were high-pass filtered at 500 Hz, and candidate spike waveforms were defined as exceeding 4 SDs of a sliding 1 s window of ongoing voltage fluctuations. Artifacts were rejected if appearing synchronously (within 0.5 ms) on over a quarter of all recorded channels. Segments of data (1.5 ms) around the time of candidate spikes were selected for spike sorting using principal component analysis through the open source spike sorting software MClust in MATLAB (A. David Redish, University of Minnesota). Sorted units were classified as single- or multiunits, and single units were validated by the presence of a clear refractory period in the autocorrelogram. LFP data were low-pass filtered at 300 Hz and downsampled to 1000 Hz.

Fixation behavior. The marmosets were trained to saccade to a marmoset face to initiate each trial. On the gaze arriving at the face, it disappeared and was replaced with a white fixation point [0.15 degrees of visual angle (DVAs)]. The marmosets held fixation on the fixation point (1.5 DVA tolerance) for a minimum duration (400 ms monkey W, 300 ms monkey T) awaiting the appearance of a drifting Gabor target (4 DVA diameter; appearing 6–7 DVAs eccentricity at 1 of 2 equally eccentric locations in the visual field contralateral to the recording array). Spontaneous data were analyzed from the period of fixation preceding the appearance of a target and excluding the initial 100 ms following fixation initiation. Early fixation breaks (defined by the excursion of the eye position from the fixation window) were excluded from analysis.

Free-viewing natural scenes. Marmosets were head fixed and their gaze monitored as in the previous task. Grayscale versions of naturalistic images (spanning 20–30 DVAs) were randomly interleaved and presented to the monkey. The monkey was free to look at the images, and after 10 s was given a juice reward. Visual activity was analyzed as in the spontaneous fixation data excluding a 250 ms window around the times of saccades. Saccades were defined as velocity peaks exceeding 25° per second. The time of saccade was taken from the peak velocity after threshold crossing. Velocity was calculated from the absolute value of the first numerical derivative of the smoothed vertical and horizontal eye traces (5 ms sliding Gaussian). We excluded from our analysis spikes that occurred from 50 ms before to 200 ms after detected saccades. Multiunit spiking activity from two recording sessions in Monkey T and one session in Monkey W (N = 142 units) were combined and analyzed as there was no significant difference in spike-phase index (SPI) effects between the monkeys (p = 0.10; Wilcoxon rank-sum test).

Spike artifact elimination . To eliminate spike artifacts from the LFP, we applied a despiking algorithm first described in Zanos et al. 2011. The goal of the algorithm is to eliminate the contribution of spike waveforms to the signal that after being downsampled and low-pass filtered constitutes the LFP. The algorithm assumes the LFP is based on the measured wideband voltage trace recorded from the electrode (y), which is composed of a low-frequency signal (the LFP, w), high-frequency spike components η^k, an offset μ, and white noise ε ad follows:

$$y = w + \sum_{k=1}^{m} \eta^k + \mu + \varepsilon. \tag{1}$$

Here, m is the number of spikes for kth neuron k. The high-frequency component of k is the convolution of the spike train s^k and the spike waveform ϕ^k as in the following:

$$\eta^k = \phi^k * s^k. \tag{2}$$

Rather than using a spike-triggered average approach to generate a mean template of the spike waveform, which is subtracted at the time of each spike, the algorithm optimally estimates the local field potential w, each spike waveform ϕ^k, and the offset μ, which adjusts for the fact that spike waveforms tend to be negative.

The first assumption is that the LFP is smooth with most of its power in the lower frequencies as follows:

$$p(w) = \mathrm{N}(0, \gamma^2\Gamma), \tag{3}$$

where $N(a, \Sigma)$ represents a multivariate Gaussian with mean a and covariance Σ, and Γ is a matrix representing the assumption of smoothness. Multiplying with some vector x (i.e., Γx) produces a low-pass filtered version of x, and γ controls the strength of the prior. The second assumption is that ε is generated by a white noise process $p(\varepsilon) = N(0, 2\mathrm{I})$. The final assumption is that the spike waveforms ϕ^k lie in a subspace B, where $\varphi^k = B\phi^k$ and the spike waveforms are described in a 1.5 ms interval around the peak depolarization. Bayesian inference was used to obtain maximum a posteriori (MAP) model parameters for the LFP w, the spike waveforms ϕ^k, and the offset μ. By Bayes's theorem, the log-posterior model is the following:

$$p(w, \phi^k, \mu|y) \propto \mathrm{p}(\mathrm{y}|\mathrm{w}, \phi^k, \mu)\ p(w)$$
$$= k\exp\left[-\frac{1}{2\sigma^2}\sum_i \left(y - w - \sum_{k=1}^{m}\eta^k - \mu\right)_i^2 - \frac{1}{2\gamma^2} w\Gamma^{-1}w\right], \tag{4}$$

where k is a constant factor. The partial derivatives with respect to the parameters are set to 0, and the log of this expression provides the MAP estimates of the parameters $\bar{w}$, $\bar{\varphi}^k$, and $\bar{\mu}$ as follows:

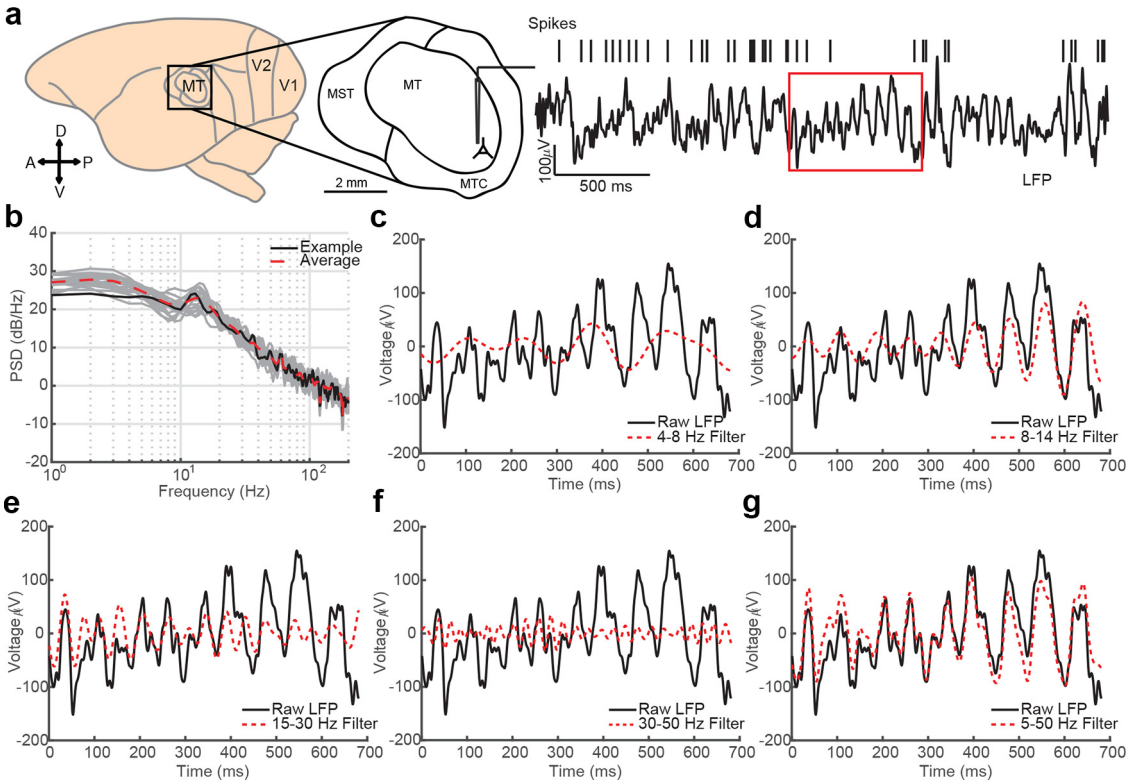

Figure 1. Cortical LFP recordings are inherently broad spectrum. ***a***, Spikes and LFPs were recorded from area MT of common marmosets while they held fixation on a blank screen. Right, Three seconds of raw LFP (filtered 1–100 Hz) and spike times from a well-isolated neuron recorded on the same electrode is plotted. The red box indicates a period of fixation during the recording epoch. ***b***, The power spectrum for the LFP trace in ***a*** is plotted in black, and 10 additional 3 s epochs are plotted in gray. The red dashed line is the mean power spectrum across trials. ***c***, The raw LFP during fixation is plotted in black against the narrowband filtered theta oscillatory component (4–8 Hz, red dotted line). ***d–f***, Same as ***c*** but for alpha (8–15 Hz), beta (15–30 Hz), and low gamma (30–50 Hz) bandpass filters. ***g***, The wideband filtered (5–50 Hz) LFP follows the dominant fluctuation in the raw LFP as it shifts in temporal frequency.

$$\bar{w} = (\gamma^2\Gamma + \sigma^2 I)^{-1}\gamma^2\Gamma\left[y - \sum_k s^k * (B\bar{\varphi}^k) - \bar{\mu}\right]$$

$$\bar{\varphi}^k = (s^k * B) + \left[y - \bar{w} - \sum_{j\neq k} s^j * (B\bar{\varphi}^j) - \bar{\mu}\right]$$

$$\bar{\mu} = \frac{1}{n}\sum_k \left[y - \bar{w} - \sum_k s^k * (B\bar{\varphi}^k)\right]. \quad (5)$$

An implementation of this algorithm in MATLAB is available from the original authors (http://apps.mni.mcgill.ca/research/cpack/lfpcode.zip).

Generalized phase. We calculated GP as described previously (Davis et al., 2020). The purpose of GP is to mitigate the breakdown of the analytic signal representation for spectrally broad signals. As an initial step in the GP representation, then, we filter the signal within a wide bandpass (i.e., 5–50 Hz; fourth-order zero-phase Butterworth filter), excluding low-frequency content that contributes to origin offsets in the complex plane that distort the estimate of phase angles for higher frequency signals. We then use the single-sided Fourier transform approach (http://www.fuchs-braun.com/media/d9140c7b3d5004fbffff8007ffffff0.pdf; Marple, 1999) on the wideband signal and compute phase derivatives as finite differences, which are calculated by multiplications in the complex plane (Feldman, 2011; Muller et al., 2014, 2016). High-frequency intrusions appear in the analytic signal representation as complex riding cycles (Feldman, 2011), which manifest as periods of negative frequencies in the analytic signal representation. As a secondary step, we then numerically detect these complex riding cycles (N_c points of negative frequency) and use shape-preserving piecewise cubic interpolation on the next $2N_c$ points following the detected negative frequency epoch. The resulting representation captures the phase of the largest fluctuation on the recording electrode at any moment in time (Fig. 1*f*), without the distortions because of the large, low-frequency intrusions or the smaller, high-frequency intrusions characteristic of the *1/f*-type fluctuations in cortical LFP (Pereda et al., 1998; Linkenkaer-Hansen et al., 2001; Milstein et al., 2009). All phase estimates of filtered LFP segments were calculated using the GP algorithm.

Spike-phase coupling. Three-second LFP epochs centered on the period of fixation were analyzed during the fixational behavioral task. The LFP segments were filtered (fourth-order zero-phase Butterworth filter with varying filter bandwidths depending on the analysis condition), and spike-phase coupling was calculated over epochs of fixation excluding the initial 100 ms following fixation initiation. The degree of spike-phase coupling was measured as the mean resultant vector length for the LFP phase distribution collected at the time of observed spikes. This measure was calculated using the circ_r function in the Circular Statistics Toolbox for MATLAB (Berens, 2009). The mean resultant vector r of the spike-phase distribution is the normalized sum over complex exponentials of the phase angles ϕ as follows:

$$r = \frac{1}{M}\sum_j^N e^{i\Phi j}, \quad (6)$$

where M is the number of spikes, and the modulus of r ($|r| \in [0, 1]$) represents the degree of spike-phase modulation. The closer the value is to zero, the more uniform the phase distribution. The closer the value is to one, the more concentrated the phases.

Filtered-raw LFP signal to noise ratio. We calculated the signal-to-noise ratio (SNR) in decibels by computing the ratio of the summed squared magnitude of the filtered LFP in either theta (4–8 Hz), alpha (8–15 Hz), beta (15–30 Hz), low gamma (30–50 Hz), or the wideband (5–50 Hz) filter to the summed squared magnitude of the broadband 1–100 Hz LFP. The SNR was calculated over a window corresponding to approximately a single cycle of the mean frequency of each filter band

(150, 75, 50, 25, and 50 ms respectively). The tested window was slid by 1/fifth the window width over the entire fixation period. Only spike times that occurred in a window that exceeded −5 dB SNR was included in the SPI calculation for that narrowband filter.

Generalized linear model analysis. To compare the relative predictive power of spike timing between multiple narrow and a single wideband measure of LFP phase (GP), we tested general linear models (GLMs) trained to predict the likelihood of spiking activity. In particular, both GLMs were trained using LFP phases recorded at points in time when spikes occurred, and an equal size sample of LFP phases, selected at random, when no spike occurred. The first model used as predictors the phase at the time of each spike or nonspike for theta (4–8 Hz), alpha (8–15 Hz), beta (15–30 Hz), and low gamma (30–50 Hz) narrowband filtered LFP. The second model used a single predictor, the narrowband beta phase (15–30 Hz), and the third model also used a single predictor, the wideband (4–50 Hz) LFP GP computed on the same training set. To linearize the circular phase variables, we used the sine and cosine of each phase value as separate predictors (Cremers and Klugkist, 2018), resulting in eight predictors for the narrowband model and two predictors for the single narrow and wideband models as follows:

$$Y_i = \kappa_0 + \kappa_1 \sin(\varphi_\theta) + \kappa_2 \cos(\varphi_\theta) + \kappa_3 \sin(\varphi_\alpha) + \kappa_4 \cos(\varphi_\alpha) + \kappa_5 \sin(\varphi_\beta) + \kappa_6 \cos(\varphi_\beta) + \kappa_7 \sin(\varphi_\gamma) + \kappa_8 \cos(\varphi_\gamma), \quad (7)$$

single narrowband GLM as follows:

$$Y_i = \kappa_0 + \kappa_1 \sin(\varphi_\beta) + \kappa_2 \cos(\varphi_\beta), \quad (8)$$

and single wideband GLM as follows:

$$Y_i = \kappa_0 + \kappa_1 \sin(\varphi_{WB}) + \kappa_2 \cos(\varphi_{WB}), \quad (9)$$

where the model output Y_i for the phases at time sample i is determined by the coefficients on the sine and cosine of the filtered LFP phase. The GLM was fitted using a binominal logit link function to relate changes in the phase predictor variables to the binary output variable at each time sample (spike or no spike). GLMs were fit to half the data in each dataset ($N = 20$ across two monkeys), and the predictor coefficients were tested on the other half of the data. The predictive power of each GLM was evaluated by measuring the area under the curve (AUC) for the receiver-operator characteristic (ROC) curve generated by comparing the true spike hit rate of each model output to the spike false alarm rate given the model output.

Simulated spike and LFP generation. To generate surrogate spiking and LFP data, we first generated a normal distribution of random frequency values with a mean of 10 Hz and a standard distribution of 1 Hz. We then generated a 100 s sinusoidal signal, whose frequency drifted with random draws from the frequency distribution. In the case where spikes were generated from the phase of this narrowband signal, we first filtered this signal between 8 and 15 Hz and used the phase to generate spike times. We also generated a broadband noise signal generated from a Gaussian distribution with mean of 0 and an SD of 1, whose power spectrum followed a $1/f$ power law (Kasdin, 1995). In the case where spikes were generated from the phase of the broadband signal, the drifting sinusoidal and pink noise signals were summed in the frequency domain and transformed back into the temporal domain and filtered between 1 and 100 Hz. The combination of the sinusoidal signal and the noise signal made up our surrogate LFP signal, which was identical between the alternative spike generating conditions.

Spike times were generated using a phase-dependent Poisson spike generator. The phase-dependent spiking probability was defined with a circular-linear function across 21 phase bins with a 0% spiking probability at 0 rad phases and a 1% spiking probability at $\pm\pi$ rad phases. At each millisecond in time, a random value was drawn from a Poisson distribution, whose lambda corresponded to the probability of a spike occurring at the phase of either the sinusoidal (narrowband hypothesis) or surrogate LFP (broadband hypothesis) signal at that millisecond. Any drawn value that exceeded zero produced a single spike time. The relative phase-dependent spike probabilities produced irregular spike trains with mean firing rates roughly between 5 and 6 Hz in both conditions. The calculation of spike-phase coupling was performed identically as that in the recorded data. The surrogate LFP was filtered in either narrow or wide filters, and the GP was drawn at the time of each spike to generate spike-phase distributions.

Statistical analysis. Statistical tests used in this study include the parametric pairwise Student's t test, the nonparametric Wilcoxon signed-rank test, and the Wilcoxon rank sum test. Two monkeys were used in this work. No power analyses were performed as the number of monkeys used followed standard conventions to reduce the number of primates required for neuroscience research. All results were consistent across both monkeys and were therefore collapsed for analysis. Individual measurements within $N = 20$ recording session were averaged, and statistical tests were performed on the averages across recording sessions.

Data Availability. The data that support the findings of this study are available from the corresponding authors on reasonable request. An open-source code repository for the generalized phase algorithm is available from http://mullerlab.github.io.

Results

We measured spike-phase coupling for single- and multiunit spiking activity across traditional narrowband and broadband filtered LFP signals. Spiking activity and LFP data were previously recorded from chronically implanted multielectrode arrays (Utah array, Blackrock Microsystems) in area MT of two common marmosets (*Callithrix jacchus*; 10 recording sessions in each monkey) as they fixated on a point on an otherwise blank screen (gray background, 75 candela/m^2; Fig. 1*a*), awaiting the appearance of a faint visual target during a challenging visual detection task (Davis et al., 2020). Similar experimental paradigms have been used to study the relationship between prestimulus oscillatory phase and sensory processing and behavioral performance (Busch et al., 2009; Balasubramanian et al., 2020; Zareian et al., 2020). The raw LFP (filtered from 1 to 100 Hz) sporadically exhibited rhythmic fluctuations across a range of time scales, but there was not a clear peak in the power spectral density that would be consistent with a clear and consistent oscillatory component (Fig. 1*b*).

The LFP during periods of fixation was filtered in classically defined frequency bands—theta (4–8 Hz), alpha (8–15 Hz), beta (15–30 Hz), and low gamma (30–50 Hz)—or in a wideband filter that spanned all of these narrow bands from 5 to 50 Hz (Fig. 1*c–g*). The bounds of the wideband filter were selected to exclude low-frequency fluctuations (<5 Hz) that are associated with slow changes in arousal (Steriade et al., 2001; Petersen et al., 2003) and high-frequency components that may be contaminated by spiking artifacts and could, therefore, induce spurious spike–LFP correlations (Ray et al., 2008a; Zanos et al., 2011). However, it could be possible spiking artifacts exist at sub-50 Hz frequencies, which could, in principle, bias our estimate of the relationship between spiking activity and LFP phase in our broadband representation. To mitigate this potential confound, we performed a despiking procedure on the data as described in Zanos et al. (2011). This removes spike waveforms from the raw (30 kHz) recorded electrode data signals through spike-waveform subtraction and interpolation before downsampling and filtering into the LFP. Any remaining relationship between the phases of sub-50 Hz activity in any frequency band must therefore be because of an indirect relationship between the population currents that give rise to the LFP and individual neuronal spiking, and not the direct contribution of that spike occurring itself.

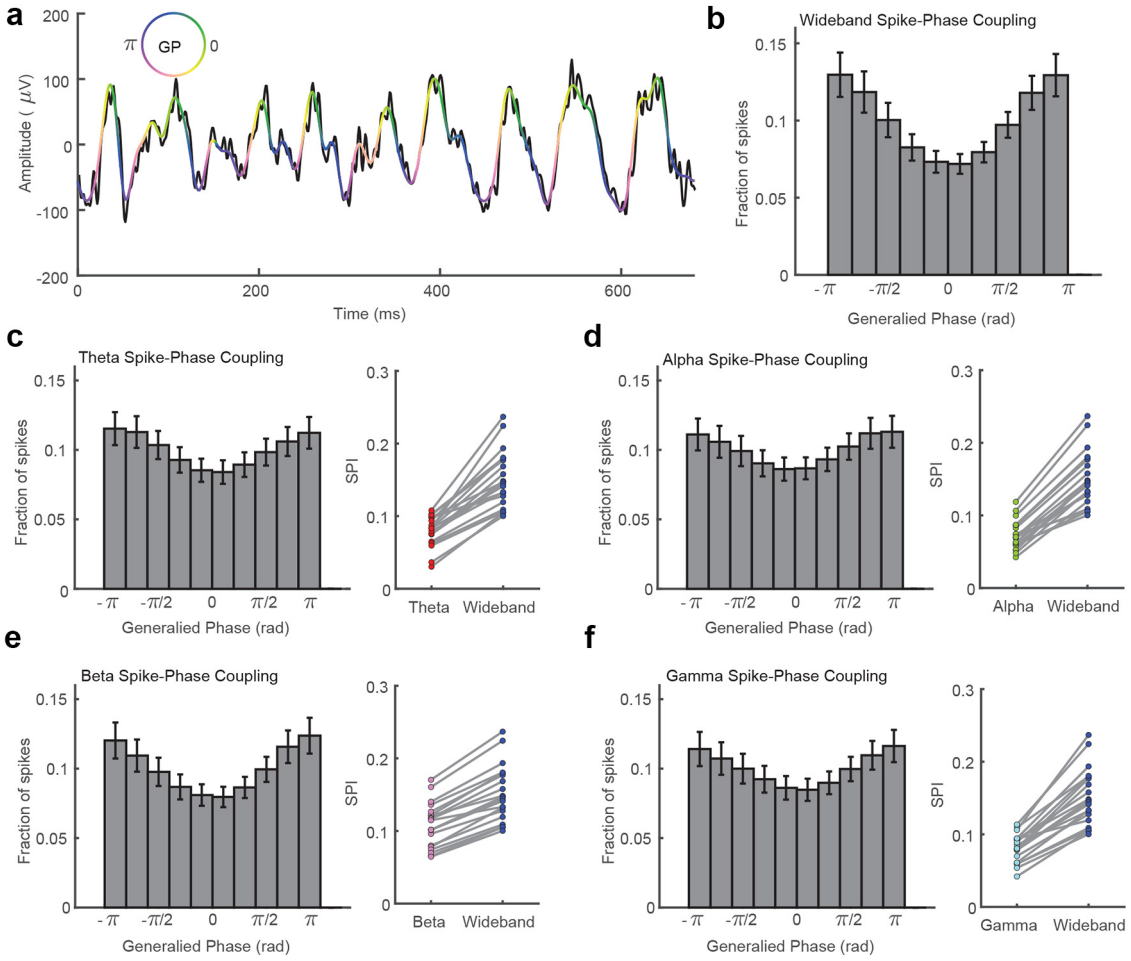

Figure 2. Spikes are more strongly coupled to the phase of wideband filtered LFP signals than narrowband oscillatory components. ***a***, The raw (5–200 Hz) filtered LFP trace from Figure 1 is plotted in black. The wideband filtered trace (5–50 Hz) is plotted in pseudocolor corresponding to the GP of the wideband filtered trace according to the color wheel. GP captures the troughs (blue/purple) and peaks (yellow/green) of the dominant fluctuations while interpolating over the higher frequency, lower amplitude riding cycles. ***b***, Histogram showing the fraction of spikes that occurred during different phases of the wideband filtered LFP (10 phase bins, $N = 20$ sessions across two monkeys. Error bars indicate SEM. ***c***, The spike-phase distribution was flatter for theta band (4–8 Hz) filtered LFP. The mean SPI, which quantifies the mean vector length of the circular distribution of spike phases, is plotted across 20 sessions from two monkeys. The wideband filtered LFP (blue) had significantly stronger SPI values than theta filtered LFP (red, $p < 1 \times 10^{-9}$, 2-tailed paired sample t test). ***d–f***, Same as ***c*** but for alpha (green, $p < 1 \times 10^{-10}$), beta (pink, $p < 1 \times 10^{-11}$), and gamma filtered LFP (cyan, $p < 1 \times 10^{-9}$).

If spiking activity is either organized into oscillations, giving rise to narrowband fluctuations in the LFP, or if LFP oscillations reflect population-wide subthreshold fluctuations that modulate the probability of spiking within a particular band, then spikes should tend to be aligned in phase with the LFP within these frequency ranges. Alternatively, if no individual rhythmic component of the LFP dictates the excitability of neurons, but rather the precise, moment-by-moment fluctuations of the LFP reflect the state of the population, we would expect spikes to occur more often at phases of the broadband LFP that correspond to states of depolarization across the local population, regardless of frequency.

To test these competing hypotheses, we measured the phase of each filtered LFP signal at the times of multiunit spiking activity. Phase is conventionally measured for oscillatory or spectrally narrow signals by calculating the analytic signal (Marple, 1999; Feldman, 2011), where instantaneous amplitude and phase can be expressed in polar coordinates and whose real and imaginary parts are related to each other by the Hilbert transform. However, for spectrally broad signals, the standard computational implementations break down (Le Van Quyen et al., 2001). Low frequencies can shift the analytic signal representation by a constant in the complex plane, distorting the estimated phase angle. In addition, high-frequency intrusions introduce complex riding cycles that generate phase reversals and appear as negative frequencies that distort the analytic signal. To address these problems, we introduced an updated approach to the analytic signal representation, termed "generalized phase" (Davis et al., 2020). Briefly, in this approach we first impose a high-pass cutoff on the signal (5 Hz). This step aims to eliminate low-frequency intrusions while also preserving a significant portion of the signal spectrum and minimizing waveform distortion. Second, we identify negative frequencies, which can arise from high-frequency intrusions, and remove them, replacing the phase values with shape-preserving interpolation. This approximates the continuation of the trajectory of the dominant fluctuation. The result, after filtering, is an estimate of phase that tracks with the dominant frequency component of the LFP as it shifts over time (Fig. 2*a*) while minimizing phase distortions that arise because of narrowband filtering a nonstationary broad spectrum signal such as the raw LFP (Yael et al., 2018). All results reported here, for both broadband and narrowband filtered data, were computed using GP. Low- and high-frequency intrusions are rare in narrowband filtered signals, so for narrowband filtered data, computation of

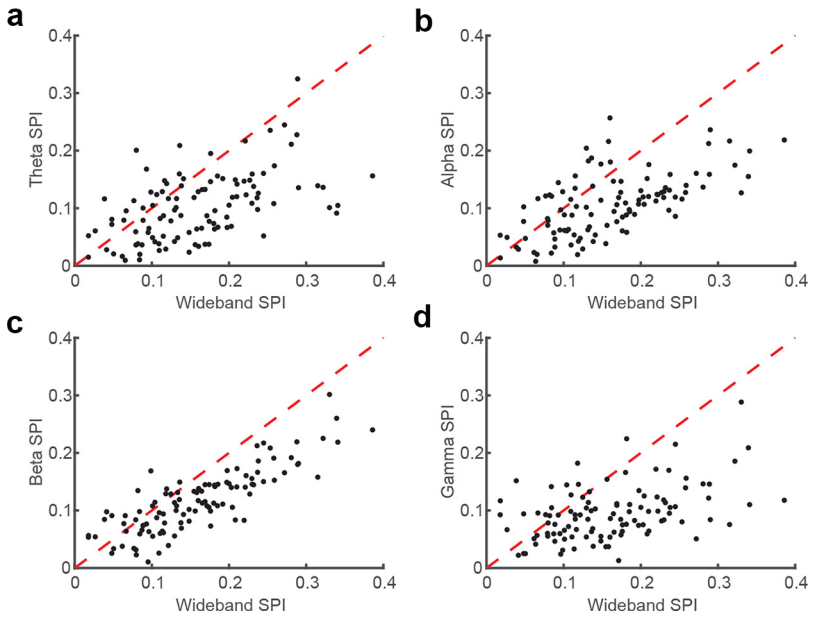

Figure 3. Stronger wideband spike-phase coupling is consistent across the population of recorded single-units. ***a***, Scatter plot comparing the magnitude of SPI after use of a broadband filter (*x*-axis) or theta band filter (*y*-axis) for each identified single unit ($N = 107$ across 20 recordings sessions). ***b–d***, Same as for ***a*** but for alpha, beta, and gamma filters. The wideband filter had a consistently stronger SPI than the narrowband filtered oscillatory phases across the population of single units.

GP should yield very similar phase estimates to those estimated using the Hilbert transform. To confirm this, all analyses were repeated for narrowband filtered signals using the Hilbert transform. As expected, the results were virtually identical. All future mentions of phase therefore refer to the GP of the signal.

The phase of the wideband filtered signal is strongly coupled to the timing of measured multiunit spiking activity (Fig. 2*b*). We measured an index of the coupling of spikes to each filtered LFP by calculating the mean resultant length of the circular spike-phase distribution. This SPI value ranges from 0 (uniform spike-phase distribution) to 1 (spikes perfectly coupled to a single phase), and for the 5–50 Hz wideband filtered signal, the average SPI was 0.15 ± 0.009 SEM ($N = 20$ sessions across two monkeys). The wideband filtered SPI was significantly stronger than the coupling observed after filtering in theta (SPI = 0.08 ± 0.005; $p < 1 \times 10^{-9}$; two-tailed paired sample *t* test), alpha (SPI = 0.07 ± 0.005; $p < 1 \times 10^{-10}$), beta (SPI = 0.11 ± 0.007; $p < 1 \times 10^{-11}$), or gamma (SPI = 0.08 ± 0.009; $p < 1 \times 10^{-9}$) frequency bands (Fig. 2*c–f*). These results suggest that the instantaneous rhythmic state of neuronal excitability is better reflected in the phase of the ensemble LFP activity rather than in the phase of any particular narrowband subcomponent.

If oscillations reflect information streams analogous to channels on a radio, then it could be the case that some neurons are more coupled to one embedded oscillation, and other neurons are more coupled to a different oscillation, and by collapsing across multiunit activity, the phase-dependence of the spiking activity is diluted for each narrowband filter. If true, we might find stronger spike-phase coupling for the wideband filter across the populations, although individual neurons are best coupled to different narrowband oscillations. To test this, we measured the spike-phase coupling across filters for well-isolated single units in our recordings. We did not find any evidence of differential preference across neurons for narrowband signals. Rather, the majority of neurons had a stronger SPI to the state of the wideband signal compared with theta (78.50%, $N = 107$ single units; Fig. 3*a*), alpha (78.50%, Fig. 3*b*), beta (83.18%, Fig. 3*c*), or gamma (85.98%, Fig. 3*c*) filtered signals. Additionally, for the minority of neurons that did show a stronger SPI to a narrowband filtered signal, they were more weakly coupled in general (average SPI = 0.09) and did not show specific preference to any one narrowband frequency. Thus, variable population phase coupling to narrowband signals could not explain why the wideband filtered signals exhibit stronger spike-phase coupling.

One possibility is that spike timing is only governed by each narrowband oscillation when that oscillation is strongly present in the data, and as each oscillation is only transiently present, it is unfair to expect, for example, gamma to predict spike timing when gamma is not present in the data. To test this we restricted our analysis to only count spikes for each frequency band at times when there is strong oscillatory power in that band. To do this we calculated the SNR between the filtered and raw (1–100 Hz) LFP and identified epochs where the narrowband signal exceeded a −5 dB threshold for at least one cycle of the center frequency of the filter bandwidth. Only spikes that occurred during these epochs were included for that narrowband SPI measure. Despite restricting each filter band to spikes that occur when those oscillations are transiently apparent in the data, the wideband measure still captures the strongest SPI values (Fig. 4*a*; wideband mean SPI = 0.16 ± 0.010 SEM; compared with theta, 0.11 ± 0.010; alpha, 0.08 ± 0.005; beta, 0.12 ± 0.010; and gamma, 0.09 ± 0.005; $p < 0.001$, Wilcoxon signed-rank test) while also describing a majority of the recorded data (approximate fraction above dB threshold; wideband 92% vs theta 16%; alpha 46%; beta 42%; and low gamma 19%).

Thus, spike timing is better predicted by broadband phase than narrowband phase for any of the bands tested. We next asked how well spike timing could be predicted based on the combination of all four narrowband filtered signals. To test this we constructed a GLM that took as its input the phase values measured over the four narrow band frequencies (spanning 4–50 Hz) at times when a spike occurred and an equal number of randomly drawn times when no spike occurred. The GLM was trained to predict whether a spike occurred, based on the four phases. The model was trained on half the data in each recording session, with the remaining data held out as a test set. The ability of the model to predict spiking was measured using ROC analysis.

We reasoned that if oscillatory activity across the multiple narrow bands drives spiking activity, the four-factor GLM, which has simultaneous access to the phases of all four oscillatory signals, should predict spiking better than a GLM trained to predict spiking based on the phase computed in an individual band (four-factor GLM AUC = 0.578 ± 0.004 SEM; single narrowband GLM AUC = 0.545 ± 0.003 SEM; $p = 0.00{,}009$, Wilcoxon signed-rank test). This analysis shows that more information about spiking is present across multiple bands. This is consistent with two different hypotheses. The first is that the narrow bands capture the individual contribution of oscillations that fall within each band, and the four-factor GLM reflects the joint contributions of these oscillatory drivers. An alternative hypothesis is that the processes that drive spiking activity fluctuate over time in

their power spectrum, and spiking activity follows these fluctuations over time, regardless of where they travel in frequency. If the first hypothesis is true, the four-factor GLM, which has access to the phase within each band, should perform better than a single-factor broadband GLM, which is provided with a single measure of phase that is blind to the interactions across the same frequency space. If the second hypothesis is true, the single-factor broadband GLM, which uses a measure of phase that tracks with the dominant LFP frequency as it changes over time, should do as well as the four-factor GLM.

To test this, a GLM was trained on the same data that was used to train the four-factor GLM, but instead of providing it with four phases computed within the four narrow bands, it was trained using only a unitary measure of phase—GP applied to the wideband (4–50 Hz) signal as its input—and its ability to predict spiking was measured using the same ROC analysis. As shown in Figure 4*b*, there was no significant difference in the ability of the combined four narrowband or one wideband GLM to predict spike times as defined by the area under the curve for each the ROC for each session (wideband mean AUC = 0.579 ± 0.005 SEM; p = 0.16, Wilcoxon signed-rank test). Thus, even when combining signals across multiple frequency bands, narrowband filtering adds no information beyond what is already present in the phase of the momentarily dominant fluctuation in the LFP preserved in the wideband representation and as measured using generalized phase.

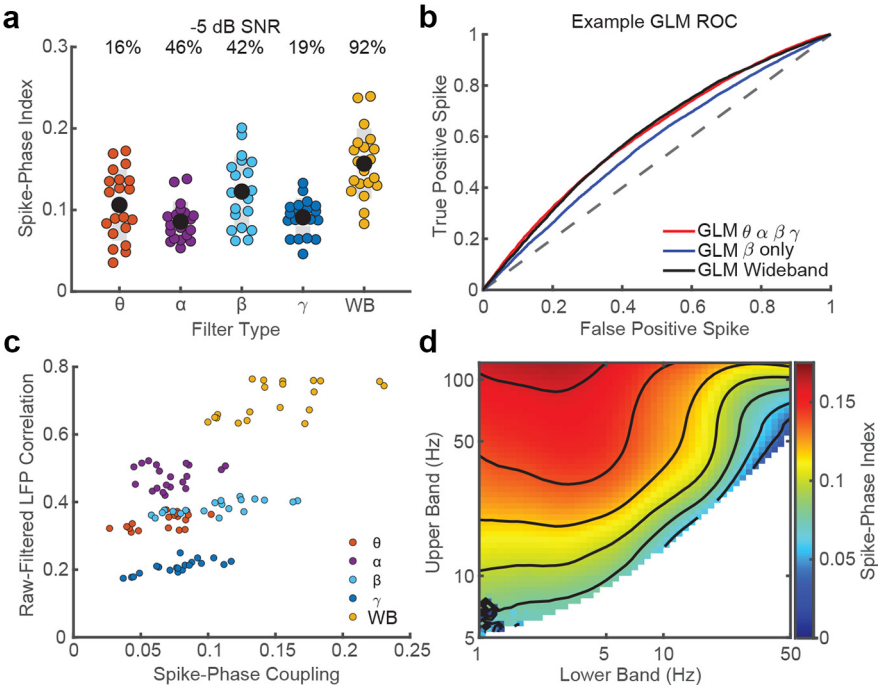

Figure 4. Narrowband signals do not contain more spike-phase information. ***a***, SPI values after restricting the inclusion of spikes to when significant power is present in each individual filter band (−5 dB SNR threshold, percentages indicate fraction of data above threshold; colored dots are N = 20 sessions from 2 monkeys; black dots are the population mean). ***b***, Representative ROC curves for GLM analyses comparing model sensitivity for identifying spike times based on phase, computed in four narrowband frequency ranges that tile the frequency space from 4 to 50 Hz (red), a single measure of narrowband oscillatory phase (blue), or the single wideband GP measure applied to the same frequency range as the four-factor GLM (black). There was no significant difference between the four-factor and wideband models in identifying spike times based on phase (Wilcoxon signed-rank test, p = 0.16), whereas the single best narrowband model was significantly weaker (beta, p = 0.00008). ***c***, Scatter plot comparing the correlation between the raw LFP and the filtered LFP signal (*y*-axis) and the SPI after filtering (*x*-axis) in each filter band. There was a significant positive correlation between SPI and how similar the raw LFP was with the signal after filtering (Pearson's r = 0.65, $p < 1 \times 10^{-12}$). ***d***, SPI for a range of bandpass filters ranging in high pass (lower band, 1–50 Hz) and low pass (upper band, 5–125 Hz). Each pixel is color coded with its average SPI across each recording session (N = 20 sessions from 2 monkeys). White pixels are filter combinations that have bandwidths <4 Hz. Black contour lines denote SPI intervals (0.02).

Our results suggest that spontaneous neuronal spiking in the neocortex is not organized by oscillatory activity but rather is modulated by fluctuations in synaptic activity that can be estimated from the instantaneous phase of the broadband LFP. If true, then SPI values should be correlated with how much filtering alters the LFP phase relative to the raw recorded LFP. To test this, we compared the strength of spike-phase coupling to each bandpass filtered signal with the degree of correlation between the LFP signal before and after filtering (Fig. 4*c*). There was a significant positive correlation between SPI and the raw-filtered LFP correlation across recording sessions (Pearson's r = 0.65 ± 0.11 95% CI, $p < 1 \times 10^{-12}$), suggesting a direct relationship between spike-phase coupling and how well the filtered LFP tracked with the raw LFP.

If spikes are more coupled to the broadband LFP than any embedded narrowband oscillation, then the optimal filter band for maximizing SPI should be one that is as broad as possible. To test for an optimal filter band, we scanned across a large parameter space varying the lower and upper bounds of the bandpass filter. The lower bound ranged from 1 to 50 Hz, and the upper bound ranged from 5 to 125 Hz with a minimum bandwidth of 4 Hz. Consistent with our prior results, the strongest spike-phase coupling was observed for filters that included the largest width of the signal spectrum, with an exception for the lowest frequencies (Fig. 4*d*). These results indicate that optimal filters for maximizing spike-phase coupling estimates span from 3 Hz in the lower band and as high as we sampled in the upper band (125 Hz), assuming spike artifacts are effectively removed from high-frequency components in the LFP. If not, a cautious step then is maintaining a low-pass filter, which serves to help mitigate spurious coupling values because of residual spike artifacts in higher frequencies.

Spiking activity can bleed into the LFP, artifactually inflating estimates of spike-phase coupling in high-frequency bands. Spike artifacts may be responsible for some gamma phase relationships with spiking activity, as the contribution of spike artifacts in the LFP had been previously observed down to 50 Hz (Ray and Maunsell, 2011; Zanos et al., 2011). To avoid this, we performed a despiking procedure and examined the consequence of that despiking on SPI estimates. A comparison of SPI values on the same data with and without despiking found that the despiking procedure significantly reduced SPI values for frequency bands that included frequencies below 50 Hz (but not below 15 Hz) such as low gamma (30–50 Hz; not despiked SPI = 0.13, $p = 1.65 \times 10^{-7}$, two-tailed Wilcoxon rank sum test), beta (15–30 Hz; SPI = 0.13, p = 0.026), and the wideband (5–50 Hz; SPI = 0.18, p = 0.009). There was no significant reduction in either

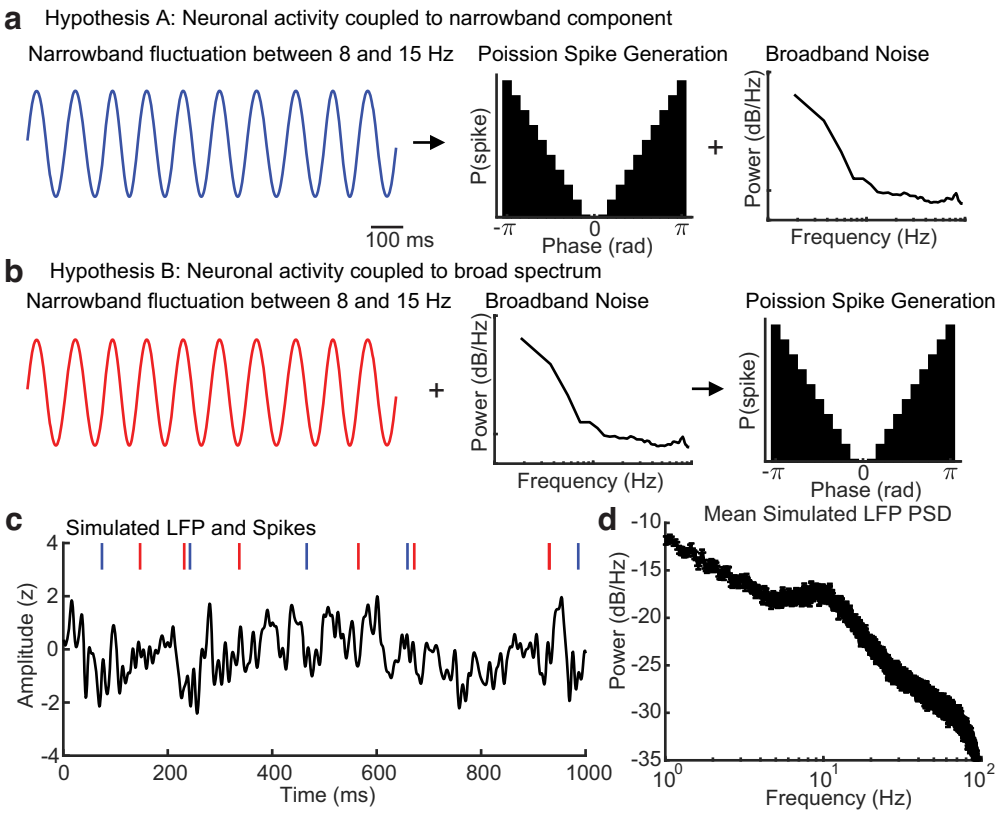

Figure 5. Two alternative hypotheses regarding the relationship between spiking activity and LFP fluctuations. ***a***, Signals generated under the hypothesis embedded narrowband fluctuations drive spiking activity. We generated a narrowband oscillatory fluctuation with power between 8 and 15 Hz. Spikes were generated with a Poisson spike generator coupled to a phase-dependent probability distribution with spikes more likely at $\pi/-\pi$ phases and less likely at 0 phases of the narrowband oscillation. This narrowband signal was added to randomly generated broadband noise to create a simulated LFP. ***b***, Signals generated under the hypothesis ensemble broadband fluctuations drive spiking activity. We generated the same narrowband oscillatory fluctuation and added the same randomly generated broadband noise as in the simulated LFP in ***a***. Spikes were then generated as in ***a*** but to the phase of the broadband simulated LFP signal. ***c***, The result of the two-signal generation paradigms is two identical simulated LFP traces but with different spike trains generated in relation to the state of either the narrow (blue raster) or broadband (red raster) signal. ***d***, The mean power spectrum across 20 simulated LFP signals. Error bars are SEM.

alpha (8–15 Hz; SPI = 0.08, p = 0.067) or theta (4–8 Hz; SPI = 0.09, p = 0.190) when we despiked the LFP. These observations are consistent with recent reports of spike artifacts having an impact on spike-LFP synchronization at frequencies as low as 20 Hz (Banaie Boroujeni et al., 2020). These results argue either that the artificial coupling of spiking activity to LFP phase may be present at low frequencies or that despiking techniques are overly liberal in the removal of spike waveforms. Regardless, even if we consider the possibility that the despiking procedure is introducing more noise than it is eliminating, the main result—that the broadband LFP phase produces the strongest SPI values—holds when this technique is not applied, and the raw data are left intact.

The results described so far are limited to spontaneous activity recorded during a period in which animals foveated a fixation point at the center of a blank screen while awaiting the appearance of a faint visual target. Do these findings generalize to more naturalistic viewing conditions? To test this, we calculated the SPI for each frequency band in animals as they freely viewed natural scene images. As the focus here is on intrinsic fluctuations, not the transient responses that are evoked at the time of the saccade, neural activity at the time of the saccade (from 50 ms before and ending 200 ms after saccades) was eliminated from analysis. Consistent with the pattern observed during fixation of a blank screen, the wideband filtered signal produced the strongest SPI values (0.16 ± 0.008; N = 142 multiunits across two sessions in Monkey T and one session in Monkey W), which was significantly stronger than the SPI values measured for theta (0.14 ± 0.007; $p < 1 \times 10^{-7}$, Wilcoxon signed-rank test), alpha (0.13 ± 0.007; $p < 1 \times 10^{-16}$), beta (0.10 ± 0.006; $p < 1 \times 10^{-14}$), and low gamma (0.11 ± 0.006; $p < 1 \times 10^{-12}$). Thus, the spontaneous coupling of spiking activity to broadband fluctuations is not limited to fixating on a blank screen but is apparent during more dynamic active vision.

Although our experimental results suggest spiking activity is better correlated with the instantaneous state of the broadband LFP rather than any individual oscillatory component, the ground truth mechanism relating spiking to rhythmic LFP activity is unknown in our recordings. To explore whether our observations can be explained by the hypothesis that spiking activity is coupled to broadband LFP phase as opposed to a narrowband oscillation, we simulated an LFP signal by combining a narrowband oscillatory fluctuation that consisted of spectral power drifting between 8 and 15 Hz with broad spectrum noise. The power spectral density of this simulated LFP fluctuation was designed to be consistent with the typical 1/f power law observed in cortical recordings *in vivo* (Miller et al., 2009; Fig. 5*d*). We then generated spike times from a Poisson spike generator, where the probability was dependent on either the phase of the narrowband 8–15 Hz oscillatory signal (Fig. 5*a*, hypothesis A) or the phase of the combined narrowband and broad spectrum signals (Fig. 5*b*, hypothesis B). Spike probability was phase dependent, with spikes most likely to occur near ± π radians and spikes least likely to occur near 0 radians. Importantly, the spectral

content of the simulated LFP was identical between the two alternative hypotheses and only the timing of spikes differed between the two conditions (Fig. 5*c*).

To recover the signal correlated with spike generation, we filtered the simulated LFP in either a narrow bandpass filter from 8 to 15 Hz, or a wide bandpass filter from 5 to 100 Hz. In the case where spikes were correlated with the phase of the narrowband oscillatory component (hypothesis A, blue), the narrowband filtered LFP signal was relatively weakly correlated with the raw simulated LFP (Pearson's r = 0.49; Fig. 6*a*). However, spike timing was strongly coupled to the phase of the narrowband filtered LFP signal (SPI = 0.34 ± 0.002 SEM; N = 20 simulations). This coupling was significantly stronger than when using the wideband filter to recover spike phases (SPI = 0.16 ± 0.002 SEM; p = < 0.0001, two-tailed Wilcoxon signed-rank test; Fig. 6*b*). In the case where the spikes were generated from the phase of the broad spectral content of the simulated LFP (hypothesis B, red), the wideband filtered LFP was strongly correlated with the raw simulated LFP (Pearson's r = 0.84, Fig. 6*c*), and the spike-phase relationship was significantly stronger after filtering in the wideband (SPI = 0.29 ± 0.002 SEM) compared with the spike-phase coupling to the narrowband filtered LFP (SPI = 0.14 ± 0.002 SEM; p = < 0.0001 two-tailed Wilcoxon signed-rank test; Fig. 6*d*). These results indicate, in principle, that if neurons were coupled to an oscillatory component, then narrowband filtering to extract that oscillation would indeed yield stronger spike-phase coupling than the broadband signal.

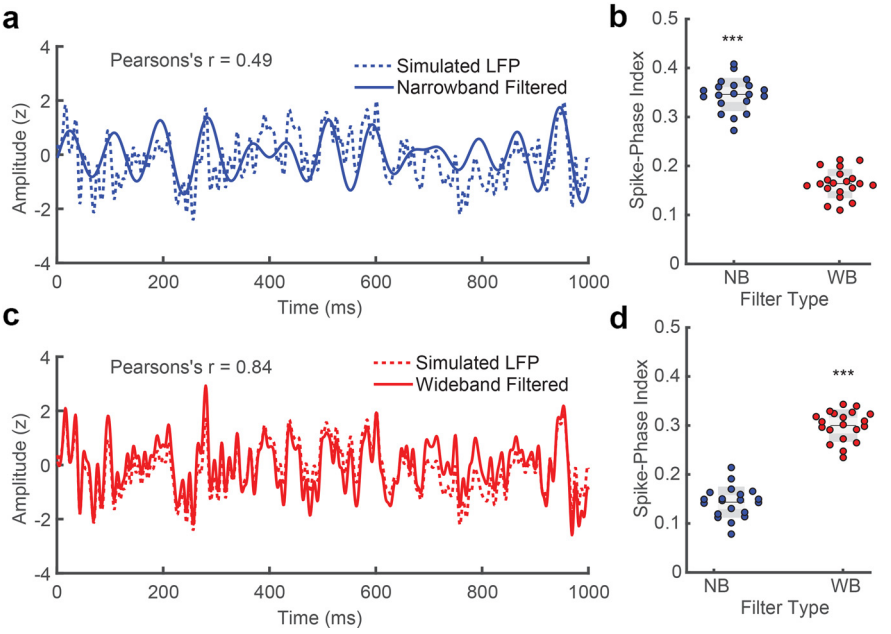

Figure 6. Spike–phase relationship is best recovered when the filter matches the signal. ***a***, The 8–15 Hz narrowband filtered LFP (solid blue line) is the recovered spike-generating signal from the ensemble simulated LFP (dotted blue line) under hypothesis A (from Figure 5). ***b***, The SPI from the phase of the narrowband signal is significantly stronger after narrowband filtering as compared with wideband filtering for the simulation where spikes were coupled to the phase of the narrowband component (5–100 Hz; N = 20 simulations; Asterisks indicate significance at p < 0.0001 2-tailed Wilcoxon signed-rank test). ***c***, The wideband filtered LFP (5–100 Hz, red line) is the recovered spike-generating signal from the broadband simulated LFP under hypothesis B (from Figure 5; dotted red line). ***d***, The SPI from the phase of the wideband is significantly stronger after wideband filtering as compared with narrowband filtering for the simulation where spikes were coupled to the phase of the broadband LFP (p < 0.0001, 2-tailed Wilcoxon signed-rank test).

We next asked whether a narrowband or broadband spike-correlated signal could reproduce the observed relationship of increasing spike-phase coupling with increasing correlation between the filtered and raw LFP signal. We filtered the signal under various filters (theta, 4–8 Hz; alpha, 8–15 Hz; beta, 15–30 Hz; and wideband, 5–50 Hz) as in the cortical recordings, as well as a broad bandpass from 1 to 100 Hz, and measured both the spike-phase coupling for narrowband and broadband correlated spike generation and the correlation between the filtered and raw LFP signal. In the case where spikes were correlated with the narrowband signal, the best filter was the 8–15 Hz filter (matching the source of the spike-generating signal), followed by the wideband and broadband filters, which each included the spike-generating signal band within its bandwidth but also included a smaller and larger part of the noise spectrum, respectively (Fig. 7*a*). In the case where spikes were correlated with the broadband signal, the best filter was the broadband filter and decreased as the filters became narrower (Fig. 7*b*). The narrowband spike source had a weak correlation between the SPI (Pearson's r = 0.27), and the degree of filter raw-signal similarity as the optimal filter was one that eliminated the broadband noise from the simulated LFP. In contrast, the broadband spike source reproduced the strong positive correlation between SPI and the filtered raw LFP similarity observed in our recordings (Pearson's r = 0.92; Fig. 7*c*). Our results indicate a that model where spikes are coupled to the state of fluctuations in the broad spectral content of the LFP is sufficient to account for our observations *in vivo* and suggest neuronal spiking is not preferentially coupled to narrowband oscillations.

Discussion

A central goal of systems neuroscience is to understand how brain activity underlies information processing and behavior. Ideally, we would like to record every action potential of every neuron and ask how they relate to one another in the service of behavior, but even with the best available neurophysiological tools—sets of electrode arrays with contacts numbering in the thousands—we can only sample a tiny fraction of the neurons in the brain. Therefore, neurophysiologists typically rely on indirect measures of the activity to estimate the spiking statistics of larger cortical populations. These include LFP, EEG, or MEG, which provide indirect measures of the activity of larger populations of neurons. Rhythmic patterns of activity are often observed in these measures, and it is common to treat these rhythmic patterns as meaningful computational units, potentially serving as independent channels of information processing, or if not independent in the context of cross-frequency phase-amplitude coupling (Munia and Aviyente, 2019), at least functionally dissociable from the signal in which they are embedded (Thut et al., 2012; Einevoll et al., 2013), similar to turning the dial on a radio to receive different streams of information.

One way of thinking about rhythmic dynamics is that the spiking probabilities of the neurons in the larger population covary within some frequency band and that this results in an

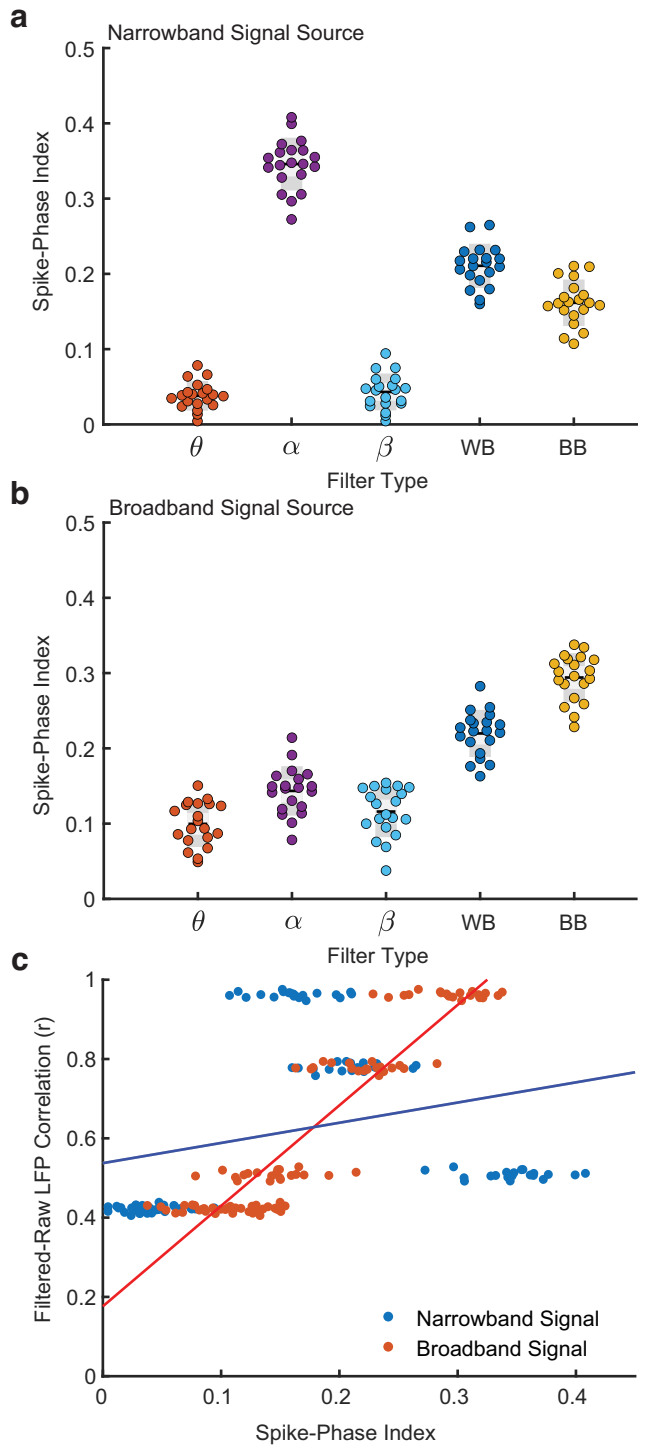

Figure 7. The model with a broadband spike correlation best matches cortical recordings. ***a***, SPI values after filtering simulated LFP in various band passes when spike times are correlated to the phase of 8–15 Hz narrowband component. In this case, the optimal filter is aligned to the signal source (8–15 Hz). ***b***, Same as ***a*** but when spike times are coupled to the phase of the broadband LFP. The pattern of SPI across filters is well matched to the pattern observed in data (Fig. 4*c*). ***c***, SPI (*x*-axis) is poorly correlated with the similarity between filtered and raw simulated LFP (*y*-axis) when spikes are correlated with narrowband signal phase (blue dots, $r^2 = 0.08$). Conversely, the correlation is strong when spikes are correlated with broadband signal phase (red dots, $r^2 = 0.85$). The relationship for a broadband signal source is well matched to the pattern observed in the cortical recordings (Fig. 4*c*).

oscillation, for the example studied here, in the LFP. If so, then by filtering the LFP within that oscillatory band and asking how it relates to some measure of either behavior (e.g., performance on a discrimination task), a neural property (such as spike timing or transmission of information across areas), or its covariation with some behavioral manipulation (e.g., directing attention into or away from the retinotopic locus of the electrode), one can identify the contribution of the oscillation to neural computations or behavior. However, there are some problems with treating neural fluctuations as oscillations. First, neural fluctuations are often only transiently rhythmic in the awake state (Jones, 2016), and even then they are not purely sinusoidal (Cole and Voytek, 2017) as they drift in frequency content from moment to moment with changes in arousal (Vinck et al., 2015), attention (Fries et al., 2001), or sensory input (Henrie and Shapley, 2005). Even in the case when neural fluctuations are strongly rhythmic, we find narrowband filtering captures less of the spike-phase relationship than when maintaining a wideband representation. This may be because the application of narrowband filters to signals that are nonstationary in their frequency content can result in a loss of timing precision in phase estimates (Yael et al., 2018).

The results presented here argue that neurons are not specifically coupled to narrowband oscillatory activity, but rather it is the state of the broadband moment-to-moment fluctuations that are informative of the relative excitability of the local population. This is not to say that rhythms are not apparent in fluctuating dynamics or that they are irrelevant for cortical function. Nor are we suggesting that rhythmic power is limited to what one would expect from stochastic synchronizations in a $1/f$ noise process. For example, it is not the case that oscillatory rhythms are only as informative as their fraction of the spectral content of broadband fluctuations. We observed that low gamma filtered signals had stronger SPI values than one might expect based on their relative power in the PSD and given how poorly correlated the gamma filtered signals were to the raw LFP. Similarly, the alpha band filtered signals had much more power and were relatively well correlated with the raw LFP yet had weaker SPI values than the beta band filtered signals, which were more poorly correlated with the raw LFP. Indeed, there is variation in the degree to which spikes couple to LFP phase across the five frequency bands studied here. However, that does not imply that those frequency bands are independent information channels, distinct from the rest of the LFP. It is evident that they are not, as we see the strongest SPI values for the broadest frequency bands.

To test what one would expect to see if it were the case spikes preferentially coupled to a narrow set of frequencies, we simulated spike trains generated from the phase of oscillatory signals embedded in an otherwise $1/f$ noise spectrum (hypothesis A). Under these conditions, we found a stronger SPI to the narrowband filter that best matched the signal underlying the spike generation signal. We also found a reduction in SPI values when the broadband filter was used. This matches what one would intuitively expect from a system composed of an oscillatory signal combined additively with a broad noise. This is the intuition that often underlies narrowband filtering approaches in electrophysiological signal analysis. Although there may be alternative explanations for why a broadband signal produces stronger SPI values in our cortical recordings, the second model, where spikes are fluctuation driven (hypothesis B), was sufficient to account for the spike-LFP coupling relationships observed in the data.

Because the phase of narrowband oscillatory activity does not predict spiking activity as well as the phase of wideband activity, it raises the question on whether and when narrowband filtering

is appropriate to study rhythmic spiking dynamics. The use of narrowband filters assumes a frequency resolved signal in the brain that is embedded in noise. As shown by hypothesis A and in Figure 6, when neural activity is strongly coupled to latent oscillatory activity, narrowband filtering is effective at recovering the signal. Therefore, in situations with steady, ongoing oscillatory activity that has low variance in frequency, such as sleep spindles, hippocampal theta, or gamma oscillations because of strong feedforward input, narrowband filtering may better capture spiking. However, if the signal is not known, narrowband filtering imposes an assumption of what is signal and noise that may not be warranted and may yield misleading results. Analytic techniques that allow for the contribution of broader frequency ranges, as used here, may reveal the degree to which results are frequency dependent or filter dependent.

It is important to note the limitations of the present findings. First, all analyses here have focused on spontaneous activity. We cannot generalize the present results to neural data collected under other conditions such as data collected during stimulus-evoked responses. Some narrowband frequency ranges, such as the gamma band, do not exhibit much power in the absence of strong sensory input (Henrie and Shapley, 2005; Ray and Maunsell, 2010). Additional experiments will be needed to determine the degree to which gamma band and generalized phase predict spike timing under these conditions. Further, the majority of the data analyzed here was recorded from the visual cortex in monkeys performing a particular task in which they foveated a fixation spot at the center of a blank screen, awaiting the appearance of a faint visual target. In our spontaneous cortical recordings, which are largely representative of the aperiodic $1/f$ power law observed in primate visual cortex (Fries et al., 2001; Henrie and Shapley, 2005; Yu and Ferster, 2010), even when oscillations are transiently present, narrowband filtering produces a weaker estimate of the spike–LFP relationship than a wider representation.

The generalized phase approach used here provides a meaningful measure of phase for spectrally broad signals (Davis et al., 2020) and reveals a stronger relationship between broadband LFP fluctuations and spiking probability than could be estimated from any individual narrowband filtered signal. The advantage of GP over narrowband signals is that it follows the moment-to-moment fluctuations in the signal and provides a phase value that generalizes across changes in frequency content. This approach can reveal patterns that would not be clear from an analysis of narrowband oscillations. For example, analysis of broadband measures of phase led to the discovery that the alignment of spontaneous traveling waves of cortical activity with the retinotopic locations of faint visual targets was predictive of the magnitude of evoked activity and perceptual sensitivity (Davis et al., 2020). These effects were only apparent in the data when the state of broadband LFP fluctuations was considered. When filtered in narrow bands, the predictive power of wave phase on behavioral performance was abolished. Consistent with those findings, the results presented here show that at least in the spontaneous waking activity of area MT, the instantaneous state of cortical populations is better estimated from the GP of broadband LFP fluctuations than from any narrowband oscillatory component. These results suggest that the phase of broadband neural fluctuations, rather than any specific narrowband frequency content, is the main influence on spontaneous spiking activity in the cortex.

References

Akam T, Kullmann DM (2010) Oscillations and filtering networks support flexible routing of information. Neuron 67:308–320.

Akam T, Kullmann DM (2014) Oscillatory multiplexing of population codes for selective communication in the mammalian brain. Nat Rev Neurosci 15:111–122.

Asaad WF, Santhanam N, McClellan S, Freedman DJ (2013) High-performance execution of psychophysical tasks with complex visual stimuli in MATLAB. J Neurophysiol 109:249–260.

Atallah BV, Scanziani M (2009) Instantaneous modulation of gamma oscillation frequency by balancing excitation with inhibition. Neuron 62:566–577.

Balasubramanian K, Papadourakis V, Liang W, Takahashi K, Best MD, Suminski AJ, Hatsopoulos NG (2020) Propagating motor cortical dynamics facilitate movement initiation. Neuron 106:526–536.e4.

Banaie Boroujeni K, Tiesinga P, Womelsdorf T (2020) Adaptive spike-artifact removal from local field potentials uncovers prominent beta and gamma band neuronal synchronization. J Neurosci Methods 330:108485.

Bartos M, Vida I, Jonas P (2007) Synaptic mechanisms of synchronized gamma oscillations in inhibitory interneuron networks. Nat Rev Neurosci 8:45–56.

Bastos AM, Vezoli J, Bosman CA, Schoffelen J-M, Oostenveld R, Dowdall JR, De Weerd P, Kennedy H, Fries P (2015) Visual areas exert feedforward and feedback influences through distinct frequency channels. Neuron 85:390–401.

Bastos AM, Donoghue JA, Brincat SL, Mahnke M, Yanar J, Correa J, Waite AS, Lundqvist M, Roy J, Brown EN, Miller EK (2021) Neural effects of propofol-induced unconsciousness and its reversal using thalamic stimulation. Elife 10:e60824.

Belluscio MA, Mizuseki K, Schmidt R, Kempter R, Buzsáki G (2012) Cross-frequency phase-phase coupling between θ and γ oscillations in the hippocampus. J Neurosci 32:423–435.

Berens P (2009) CircStat: a MATLAB toolbox for circular statistics. J Stat Soft 31:1–21.

Berger H (1929) Über das Elektrenkephalogramm des Menschen. Archiv f Psychiatrie 87:527–570.

Bitzenhofer SH, Ahlbeck J, Wolff A, Simon Wiegert J, Gee CE, Oertner TG, Hanganu-Opatz IL (2017) Layer-specific optogenetic activation of pyramidal neurons causes beta–gamma entrainment of neonatal networks. Nat Commun 8:14563.

Bonnefond M, Kastner S, Jensen O (2017) Communication between brain areas based on nested oscillations. eNeuro 4:ENEURO.0153-16.2017.

Brunel N, Wang X-J (2003) What determines the frequency of fast network oscillations with irregular neural discharges? I. Synaptic dynamics and excitation-inhibition balance. J Neurophysiol 90:415–430.

Busch NA, VanRullen R (2010) Spontaneous EEG oscillations reveal periodic sampling of visual attention. Proc Natl Acad Sci U S A 107:16048–16053.

Busch NA, Dubois J, VanRullen R (2009) The phase of ongoing EEG oscillations predicts visual perception. J Neurosci 29:7869–7876.

Buzsáki G (2002) Theta oscillations in the hippocampus. Neuron 33:325–340.

Buzsáki G, Draguhn A (2004) Neuronal oscillations in cortical networks. Science 304:1926–1929.

Buzsáki G, Wang X-J (2012) Mechanisms of gamma oscillations. Annu Rev Neurosci 35:203–225.

Buzsáki G, Anastassiou CA, Koch C (2012) The origin of extracellular fields and currents — EEG, ECoG, LFP and spikes. Nat Rev Neurosci 13:407–420.

Canolty RT, Ganguly K, Kennerley SW, Cadieu CF, Koepsell K, Wallis JD, Carmena JM (2010) Oscillatory phase coupling coordinates anatomically dispersed functional cell assemblies. Proc Natl Acad Sci U S A 107:17356–17361.

Cole SR, Voytek B (2017) Brain oscillations and the importance of waveform shape. Trends Cogn Sci 21:137–149.

Colgin LL, Denninger T, Fyhn M, Hafting T, Bonnevie T, Jensen O, Moser M-B, Moser EI (2009) Frequency of gamma oscillations routes flow of information in the hippocampus. Nature 462:353–357.

Contreras D, Destexhe A, Sejnowski TJ, Steriade M (1997) Spatiotemporal patterns of spindle oscillations in cortex and thalamus. J Neurosci 17:1179–1196.

Cremers J, Klugkist I (2018) One direction? A tutorial for circular data analysis using R With examples in cognitive psychology. Front Psychol 9:2040.

Crone NE, Sinai A, Korzeniewska A (2006) High-frequency gamma oscillations and human brain mapping with electrocorticography. Prog Brain Res 159:275–295.

Davis ZW, Muller L, Martinez-Trujillo J, Sejnowski T, Reynolds JH (2020) Spontaneous travelling cortical waves gate perception in behaving primates. Nature 587:432–436.

Destexhe A, Rudolph M, Fellous JM, Sejnowski TJ (2001) Fluctuating synaptic conductances recreate *in vivo*-like activity in neocortical neurons. Neuroscience 107:13–24.

Donoghue JP, Sanes JN, Hatsopoulos NG, Gaál G (1998) Neural discharge and local field potential oscillations in primate motor cortex during voluntary movements. J Neurophysiol 79:159–173.

Einevoll GT, Kayser C, Logothetis NK, Panzeri S (2013) Modelling and analysis of local field potentials for studying the function of cortical circuits. Nat Rev Neurosci 14:770–785.

Escobar Sanabria D, Johnson LA, Yu Y, Busby Z, Nebeck S, Zhang J, Harel N, Johnson MD, Molnar GF, Vitek JL (2020) Real-time suppression and amplification of frequency-specific neural activity using stimulation evoked oscillations. Brain Stimul 13:1732–1742.

Feldman M (2011) Hilbert transform in vibration analysis. Mech Syst Signal Process 25:735–802.

Fiebelkorn IC, Kastner S (2019) A rhythmic theory of attention. Trends Cogn Sci 23:87–101.

Flores FJ, Hartnack KE, Fath AB, Kim S-E, Wilson MA, Brown EN, Purdon PL (2017) Thalamocortical synchronization during induction and emergence from propofol-induced unconsciousness. Proc Natl Acad Sci U S A 114:E6660–E6668.

Fries P (2015) Rhythms for cognition: communication through coherence. Neuron 88:220–235.

Fries P, Reynolds JH, Rorie AE, Desimone R (2001) Modulation of oscillatory neuronal synchronization by selective visual attention. Science 291:1560–1563.

Fries P, Womelsdorf T, Oostenveld R, Desimone R (2008) The effects of visual stimulation and selective visual attention on rhythmic neuronal synchronization in macaque area V4. J Neurosci 28:4823–4835.

Friston KJ, Bastos AM, Pinotsis D, Litvak V (2015) LFP and oscillations—what do they tell us? Curr Opin Neurobiol 31:1–6.

Gao R, Peterson EJ, Voytek B (2017) Inferring synaptic excitation/inhibition balance from field potentials. Neuroimage 158:70–78.

Geller AS, Burke JF, Sperling MR, Sharan AD, Litt B, Baltuch GH, Lucas TH 2nd, Kahana MJ (2014) Eye closure causes widespread low-frequency power increase and focal gamma attenuation in the human electrocorticogram. Clin Neurophysiol 125:1764–1773.

Gregoriou GG, Gotts SJ, Zhou H, Desimone R (2009) High-frequency, long-range coupling between prefrontal and visual cortex during attention. Science 324:1207–1210.

Haegens S, Nácher V, Luna R, Romo R, Jensen O (2011) α-Oscillations in the monkey sensorimotor network influence discrimination performance by rhythmical inhibition of neuronal spiking. Proc Natl Acad Sci U S A 108:19377–19382.

Haider B, Schulz DPA, Häusser M, Carandini M (2016) Millisecond coupling of local field potentials to synaptic currents in the awake visual cortex. Neuron 90:35–42.

Henrie JA, Shapley R (2005) LFP power spectra in V1 cortex: the graded effect of stimulus contrast. J Neurophysiol 94:479–490.

Hoppensteadt FC, Izhikevich EM (1998) Thalamo-cortical interactions modeled by weakly connected oscillators: could the brain use FM radio principles? Biosystems 48:85–94.

Isaacson JS, Scanziani M (2011) How inhibition shapes cortical activity. Neuron 72:231–243.

Jensen O, Tesche CD (2002) Frontal theta activity in humans increases with memory load in a working memory task. Eur J Neurosci 15:1395–1399.

Jensen O, Mazaheri A (2010) Shaping functional architecture by oscillatory alpha activity: gating by inhibition. Front Hum Neurosci 4:186.

Jones SR (2016) When brain rhythms aren't "rhythmic": implication for their mechanisms and meaning. Curr Opin Neurobiol 40:72–80.

Kasdin NJ (1995) Discrete simulation of colored noise and stochastic processes and 1/f/sup α/power law noise generation. Proc IEEE 83:802–827.

Katzner S, Nauhaus I, Benucci A, Bonin V, Ringach DL, Carandini M (2009) Local origin of field potentials in visual cortex. Neuron 61:35–41.

Khamechian MB, Kozyrev V, Treue S, Esghaei M, Daliri MR (2019) Routing information flow by separate neural synchrony frequencies allows for "functionally labeled lines" in higher primate cortex. Proc Natl Acad Sci U S A 116:12506–12515.

Kirov R, Weiss C, Siebner HR, Born J, Marshall L (2009) Slow oscillation electrical brain stimulation during waking promotes EEG theta activity and memory encoding. Proc Natl Acad Sci U S A 106:15460–15465.

Le Van Quyen M, Foucher J, Lachaux J, Rodriguez E, Lutz A, Martinerie J, Varela FJ (2001) Comparison of Hilbert transform and wavelet methods for the analysis of neuronal synchrony. J Neurosci Methods 111:83–98.

Lindén H, Tetzlaff T, Potjans TC, Pettersen KH, Grün S, Diesmann M, Einevoll GT (2011) Modeling the spatial reach of the LFP. Neuron 72:859–872.

Linkenkaer-Hansen K, Nikouline VV, Palva JM, Ilmoniemi RJ (2001) Long-range temporal correlations and scaling behavior in human brain oscillations. J Neurosci 21:1370–1377.

Lisman JE, Idiart MA (1995) Storage of 7 +/- 2 short-term memories in oscillatory subcycles. Science 267:1512–1515.

Logothetis NK (2003) The underpinnings of the BOLD functional magnetic resonance imaging signal. J Neurosci 23:3963–3971.

Lu Y, Truccolo W, Wagner FB, Vargas-Irwin CE, Ozden I, Zimmermann JB, May T, Agha NS, Wang J, Nurmikko AV (2015) Optogenetically induced spatiotemporal gamma oscillations and neuronal spiking activity in primate motor cortex. J Neurophysiol 113:3574–3587.

Lundqvist M, Herman P, Warden MR, Brincat SL, Miller EK (2018) Gamma and beta bursts during working memory readout suggest roles in its volitional control. Nat Commun 9:394.

Marple L (1999) Computing the discrete-time "analytic" signal via FFT. IEEE Trans Signal Process 47:2600–2603.

Martin KAC, Schröder S (2016) Phase locking of multiple single neurons to the local field potential in Cat V1. J Neurosci 36:2494–2502.

McGinley MJ, David SV, McCormick DA (2015) Cortical membrane potential signature of optimal states for sensory signal detection. Neuron 87:179–192.

Merker B (2013) Cortical gamma oscillations: the functional key is activation, not cognition. Neurosci Biobehav Rev 37:401–417.

Miller KJ, Sorensen LB, Ojemann JG, den Nijs M (2009) Power-law scaling in the brain surface electric potential. PLoS Comput Biol 5:e1000609.

Milstein J, Mormann F, Fried I, Koch C (2009) Neuronal shot noise and Brownian 1/f2 behavior in the local field potential. PLoS One 4:e4338.

Misselhorn J, Schwab BC, Schneider TR, Engel AK (2019) Synchronization of sensory gamma oscillations promotes multisensory communication. eNeuro 6:ENEURO.0101-19.2019.

Muller L, Reynaud A, Chavane F, Destexhe A (2014) The stimulus-evoked population response in visual cortex of awake monkey is a propagating wave. Nat Commun 5:3675.

Muller L, Piantoni G, Koller D, Cash SS, Halgren E, Sejnowski TJ (2016) Rotating waves during human sleep spindles organize global patterns of activity that repeat precisely through the night. Elife 5:e17267.

Munia TTK, Aviyente S (2019) Time-frequency based phase-amplitude coupling measure for neuronal oscillations. Sci Rep 9:12441.

Panagiotaropoulos TI, Deco G, Kapoor V, Logothetis NK (2012) Neuronal discharges and gamma oscillations explicitly reflect visual consciousness in the lateral prefrontal cortex. Neuron 74:924–935.

Panzeri S, Brunel N, Logothetis NK, Kayser C (2010) Sensory neural codes using multiplexed temporal scales. Trends Neurosci 33:111–120.

Pereda E, Gamundi A, Rial R, González J (1998) Non-linear behaviour of human EEG: fractal exponent versus correlation dimension in awake and sleep stages. Neurosci Lett 250:91–94.

Pesaran B, Pezaris JS, Sahani M, Mitra PP, Andersen RA (2002) Temporal structure in neuronal activity during working memory in macaque parietal cortex. Nat Neurosci 5:805–811.

Pesaran B, Vinck M, Einevoll GT, Sirota A, Fries P, Siegel M, Truccolo W, Schroeder CE, Srinivasan R (2018) Investigating large-scale brain dynamics using field potential recordings: analysis and interpretation. Nat Neurosci 21:903–919.

Petersen CCH, Hahn TTG, Mehta M, Grinvald A, Sakmann B (2003) Interaction of sensory responses with spontaneous depolarization in layer 2/3 barrel cortex. Proc Natl Acad Sci U S A 100:13638–13643.

Poo C, Isaacson JS (2009) Odor representations in olfactory cortex: "sparse" coding, global inhibition, and oscillations. Neuron 62:850–861.

Purdon PL, Pierce ET, Mukamel EA, Prerau MJ, Walsh JL, Wong KFK, Salazar-Gomez AF, Harrell PG, Sampson AL, Cimenser A, Ching S, Kopell NJ, Tavares-Stoeckel C, Habeeb K, Merhar R, Brown EN (2013) Electroencephalogram signatures of loss and recovery of consciousness from propofol. Proc Natl Acad Sci U S A 110:E1142–E1151.

Ray S, Maunsell JHR (2010) Differences in gamma frequencies across visual cortex restrict their possible use in computation. Neuron 67:885–896.

Ray S, Maunsell JHR (2011) Different origins of gamma rhythm and high-gamma activity in macaque visual cortex. PLoS Biol 9:e1000610.

Ray S, Hsiao SS, Crone NE, Franaszczuk PJ, Niebur E (2008a) Effect of stimulus intensity on the spike-local field potential relationship in the secondary somatosensory cortex. J Neurosci 28:7334–7343.

Ray S, Crone NE, Niebur E, Franaszczuk PJ, Hsiao SS (2008b) Neural correlates of high-gamma oscillations (60–200 Hz) in macaque local field potentials and their potential implications in electrocorticography. J Neurosci 28:11526–11536.

Rubino D, Robbins KA, Hatsopoulos NG (2006) Propagating waves mediate information transfer in the motor cortex. Nat Neurosci 9:1549–1557.

Sanes JN, Donoghue JP (1993) Oscillations in local field potentials of the primate motor cortex during voluntary movement. Proc Natl Acad Sci U S A 90:4470–4474.

Scheffer-Teixeira R, Tort AB (2016) On cross-frequency phase-phase coupling between theta and gamma oscillations in the hippocampus. Elife 5:e20515.

Singer W, Gray CM (1995) Visual feature integration and the temporal correlation hypothesis. Annu Rev Neurosci 18:555–586.

Souza BC, Tort ABL (2017) Asymmetry of the temporal code for space by hippocampal place cells. Sci Rep 7:8507.

Steriade M, Timofeev I, Grenier F (2001) Natural waking and sleep states: a view from inside neocortical neurons. J Neurophysiol 85:1969–1985.

Strüber M, Sauer J-F, Bartos M (2022) Parvalbumin expressing interneurons control spike-phase coupling of hippocampal cells to theta oscillations. Sci Rep 12:1362.

Takahashi M, Nishida H, Redish AD, Lauwereyns J (2014) Theta phase shift in spike timing and modulation of gamma oscillation: a dynamic code for spatial alternation during fixation in rat hippocampal area CA1. J Neurophysiol 111:1601–1614.

Teleńczuk B, Dehghani N, Le Van Quyen M, Cash SS, Halgren E, Hatsopoulos NG, Destexhe A (2017) Local field potentials primarily reflect inhibitory neuron activity in human and monkey cortex. Sci Rep 7:40211.

Thut G, Miniussi C, Gross J (2012) The functional importance of rhythmic activity in the brain. Curr Biol 22:R658–R663.

Tingley D, Alexander AS, Quinn LK, Chiba AA, Nitz D (2018) Multiplexed oscillations and phase rate coding in the basal forebrain. Sci Adv 4:eaar3230.

van Kerkoerle T, Self MW, Dagnino B, Gariel-Mathis M-A, Poort J, van der Togt C, Roelfsema PR (2014) Alpha and gamma oscillations characterize feedback and feedforward processing in monkey visual cortex. Proc Natl Acad Sci U S A 111:14332–14341.

van Vugt MK, Schulze-Bonhage A, Litt B, Brandt A, Kahana MJ (2010) Hippocampal gamma oscillations increase with memory load. J Neurosci 30:2694–2699.

Vinck M, Batista-Brito R, Knoblich U, Cardin JA (2015) Arousal and locomotion make distinct contributions to cortical activity patterns and visual encoding. Neuron 86:740–754.

Voytek B, Kramer MA, Case J, Lepage KQ, Tempesta ZR, Knight RT, Gazzaley A (2015) Age-related changes in 1/f neural electrophysiological noise. J Neurosci 35:13257–13265.

Wang X-J (2010) Neurophysiological and computational principles of cortical rhythms in cognition. Physiol Rev 90:1195–1268.

Womelsdorf T, Schoffelen J-M, Oostenveld R, Singer W, Desimone R, Engel AK, Fries P (2007) Modulation of neuronal interactions through neuronal synchronization. Science 316:1609–1612.

Worden MS, Foxe JJ, Wang N, Simpson GV (2000) Anticipatory biasing of visuospatial attention indexed by retinotopically specific alpha-band electroencephalography increases over occipital cortex. J Neurosci 20:RC63.

Yael D, Vecht JJ, Bar-Gad I (2018) Filter-based phase shifts distort neuronal timing information. eNeuro 5:ENEURO.0261-17.2018.

Yu J, Ferster D (2010) Membrane potential synchrony in primary visual cortex during sensory stimulation. Neuron 68:1187–1201.

Zanos TP, Mineault PJ, Pack CC (2011) Removal of spurious correlations between spikes and local field potentials. J Neurophysiol 105:474–486.

Zareian B, Maboudi K, Daliri MR, Abrishami Moghaddam H, Treue S, Esghaei M (2020) Attention strengthens across-trial pre-stimulus phase coherence in visual cortex, enhancing stimulus processing. Sci Rep 10:4837.

Zutshi I, Brandon MP, Fu ML, Donegan ML, Leutgeb JK, Leutgeb S (2018) Hippocampal neural circuits respond to optogenetic pacing of theta frequencies by generating accelerated oscillation frequencies. Curr Biol 28:1179–1188.e3.